Nickel Loaded into Three-Dimensional Porous Composite Materials Doped by Nitrogen Atoms for Accelerating the Conversion Process of Polysulfides

Jixin Lu[1,2,3], Mengyuan Zhu[1,2,3] Lukuan Wang[1,3], Yangyang Cui[1,3], Chunjie Wu[1,3], Qiaoling Bi[1,3], Shaoyu Jiang[1,3], Qing Zhao[1,2,3], Jianxin Zhao[1,3], Linjing Liu[1,3], Cunguo Wang[1,3,*] and Aihua He[1,3,*]

[1]*State Key Laboratory of Advanced Optical Polymer and Manufacturing Technology, Key Laboratory of Rubber-plastics, Ministry of Education, Shandong Key Laboratory of High Performance Polyolefin Materials and Recycling, Qingdao University of Science and Technology, Qingdao, Shandong 266042, China*

[2]*Department of JBNU-KIST Industry-Academia Convergence Research, Jeonbuk National University, Jeonju 54896, Republic of Korea*

[3]*Enchem Tianrun New Energy Materials (Shandong) Co., Ltd., Zaozhuang 277800, Shandong Province, China*

Abstract: The industrial deployment of lithium–sulfur batteries remains hindered by sulfur's intrinsically low electrical conductivity and the pronounced shuttle effect that arises during cycling. In this study, a novel porous composite material (GA/Ni-CN) was prepared by loading the nickel metal catalyst onto nitrogen-doped three-dimensional graphene aerogel carbon-based materials. Graphene aerogel and ZIF-derived nitrogen-doped carbon framework composites provide abundant polar sites while maintaining a stable three-dimensional porous structure, enhancing polysulfide adsorption. A small amount of metallic nickel phase serves as the electrocatalytic center, accelerating the redox conversion of polysulfides while preventing catalyst overconsumption. The battery assembled with S@GA/Ni-CN as the cathode material exhibits excellent electrochemical performance and shows high electrochemistry response in cyclic voltammetry testing. In addition, the initial discharge specific capacity got to 1482 mAh/g at 0.2 C current density, substantially surpassing the sulfur utilization efficiency of conventional carbon-based materials.

Keywords: Shuttle effect, ZIF-8, Metal organic framework materials, Lithium sulfur batteries, Composite materials.

1. INTRODUCTION

Compared to commercial lithium-ion batteries (LIBs), lithium-sulfur batteries (LSBs) offer several advantages such as high energy density (2600 Wh/kg), low cost, and environmental friendliness, making them one of the most promising candidates for next-generation energy storage [1-5]. However, several limitations remain, such as the poor conductivity of elemental sulfur and the lithium polysulfide (Li_2S_X, x≥2) formed during discharge [6-8]. Additionally, significant volume expansion occurs during charging and discharging, along with pronounced shuttle effects, all of which severely hinder the industrialization of LSBs [9, 10]. To address the aforementioned issues, researchers have proposed numerous solution strategies [11, 12]. The most common approach involves introducing carbon materials such as carbon nanotubes, graphene, and porous carbon [13, 17]. While these materials offer high conductivity, their weak physical interactions with polar polysulfides result in insufficient binding strength, failing to effectively suppress the shuttle effect [18, 19]. To improve polysulfide immobilization, researchers have explored heteroatom doping such as nitrogen, phosphorus, and oxygen into the host material to enhance its adsorption capacity for polysulfides [20, 23]. However, non-metallic carbon elements exhibit relatively low binding energies with polysulfides, typically below 1.5 eV. In contrast, certain metal compounds (such as ZrO_2) demonstrate stronger binding capabilities toward polysulfides, which can enhance the battery's cycling stability to some extent [24-26]. Nevertheless, these metal compounds generally possess poor electrical conductivity, thereby slowing down the redox kinetics of LSBs [26, 27].

Generally, carbon materials with high porosity, electrical conductivity, and tunable pore sizes are considered as ideal sulfur host materials [28]. Among them, metal-organic frameworks (MOFs) have drawn substantial research interest due to their structural versatility and compatibility with these requirements [29-31]. Upon high-temperature pyrolysis, MOFs not only achieve improved electrical conductivity but also exhibit strong polysulfide adsorption capability, due to their high heteroatom content [32-35]. Furthermore, metals such as iron, cobalt, and nickel exhibit high

*Address correspondence to this author at the State Key Laboratory of Advanced Optical Polymer and Manufacturing Technology, Key Laboratory of Rubber-plastics, Ministry of Education, Shandong Key Laboratory of High Performance Polyolefin Materials and Recycling, Qingdao University of Science and Technology, Qingdao, Shandong 266042, China;
E-mail: cgwang789@qq.com

Received on 12-11-2025 Accepted on 20-12-2025 Published on 29-12-2025

E-ISSN: 2311-8717/25

catalytic activity toward redox reactions in Li-S batteries, accelerating the conversion kinetics of lithium polysulfides while strongly adsorbing polysulfides [36, 37]. Transition metal-based catalysts can accelerate polysulfide conversion and lithium sulfide (Li_2S) decomposition, thereby demonstrating high activity in Li/S batteries. He *et al*. theoretically demonstrated that transition metal d-orbital electrons can hybridize with p-orbital electrons in polysulfides, altering their electronic structure [1, 38]. This accelerates polysulfide conversion processes and lowers the decomposition barrier for lithium sulfide [39], highlighting the catalytic role of transition metals in facilitating redox processes throughout charge–discharge cycling [40].

In this study, freeze-drying and solvothermal synthesis were employed to integrate nickel metal catalysts onto a composite composed of a zeolitic imidazolate framework (ZIF) and graphene oxide. After high-temperature carbonization, Ni atoms become uniformly dispersed throughout the nitrogen-rich porous matrix, forming an efficient sulfur host material suitable for Li–S batteries. The resulting carbonized structure exhibits a well-developed porous network that effectively prevents Ni catalyst agglomeration. This material provides several key advantages: Graphene aerogel serves as a three-dimensional lightweight conductive framework with excellent mechanical toughness; the ZIF-derived nitrogen-doped carbon framework provides abundant polar sites to enhance polysulfide adsorption; while the metallic Ni phase acts as the electrocatalytic center, accelerating the redox conversion of polysulfides. Electrochemical performance testing revealed an initial discharge capacity of 1482 mAh/g at a 0.2 C rate. After 100 cycles, the reversible capacity remained at 824.6 mAh/g. In addition, GA was synthesized from graphite, an abundant precursor material, through oxidation and freeze-drying, featuring a straightforward synthesis process. ZIF-8 undergoes high-temperature carbonization to transform into a nitrogen-rich porous carbon framework, forming a stable structure dominated by carbon materials with extended service life. Furthermore, the system incorporates only a minimal amount of Ni as the catalytic component, reducing the consumption of critical metals. Subsequent chemical methods can be employed to recover the nickel metal. This carbon-based framework is also compatible with existing recycling strategies and holds potential for future expansion to biomass or biomimetic carbon sources.

2. RESULTS AND DISCUSSION

2.1. Structural Characterization

The synthesis process of the GA/Ni-CN composite material is shown in Figure **1**. First, porous GA material was prepared via freeze-drying. Subsequently, it was combined with Ni-ZIF-8 material through hydrothermal reaction to obtain GA/Ni-ZIF-8. Finally, after high-temperature carbonization for 3 hours in an argon atmosphere, yielding the GA/Ni-CN composite material.

The field emission scanning electron microscopy (FE-SEM) morphology analysis of aerogel (GA) and GA/Ni-CN is shown in Figure **2**. Figure **2a** clearly reveals the graphene oxide (GO) layered structure within GA, featuring significant interlayer spacing that facilitates subsequent adsorption and loading of sulfur atoms. Figures **2b-d** present SEM images of GA/Ni-CN material at different magnifications. Under the action of surfactants, a uniform network structure formed by

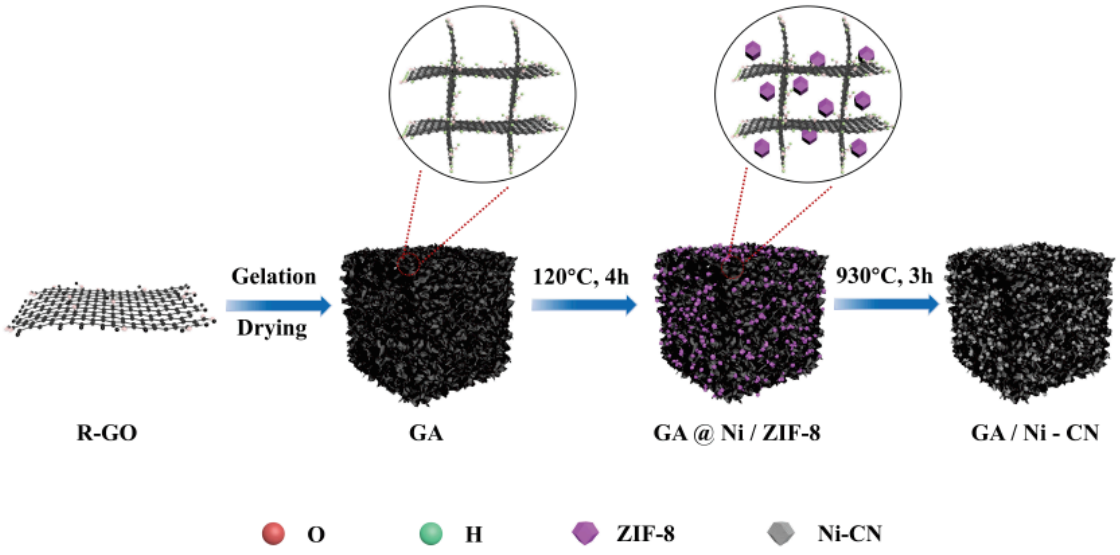

Figure 1: Schematic illustration of the procedure for the synthesis of GA/HNBRL.

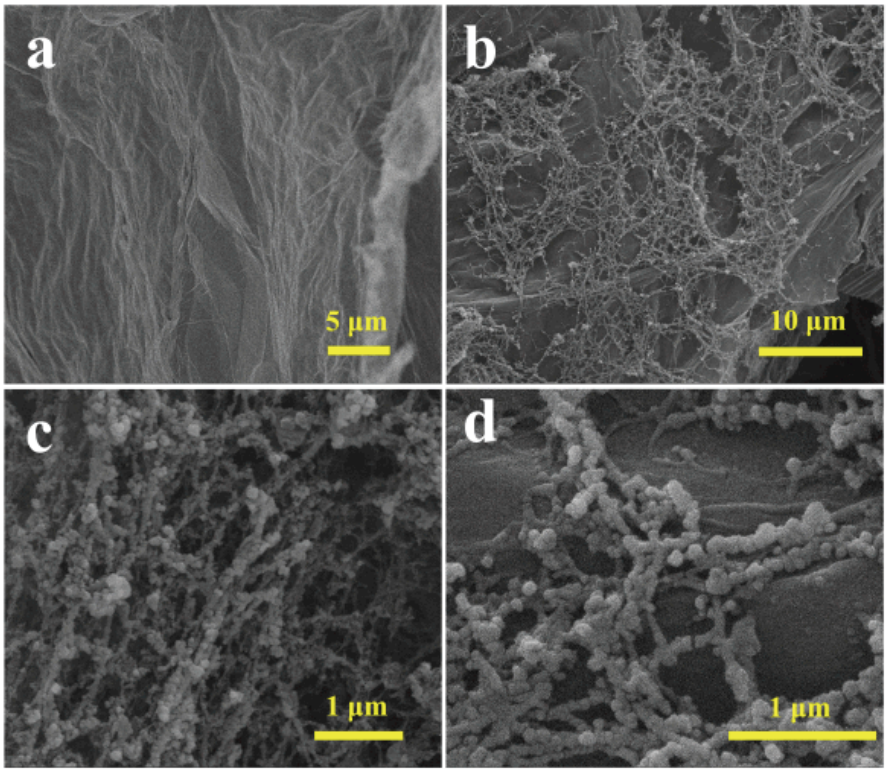

Figure 2: SEM images of GA (**a**) and GA/Ni-CN (**b**, **c**, **d**).

interconnected Ni-CN particles adheres to the GO layers within GA. This architecture provides abundant ion-transport channels and porous pathways for charge transfer, thereby significantly enhancing both electron and lithium-ion mobility. In addition, at the interface level, significant interactions exist between the graphene aerogel skeleton, nitrogen-doped carbon framework, and nickel nanoparticles. The nitrogen-rich carbon matrix provides effective coordination anchor sites for nickel species, suppressing the agglomeration of nickel nanoparticles during high-temperature carbonization and electrochemical cycling. Simultaneously, the close contact between nickel nanoparticles and the conductive carbon framework enhances interfacial electron transport, facilitating the catalytic conversion of polysulfides. The interconnected graphene aerogel further ensures continuous electronic conduction pathways and overall mechanical connectivity, thereby constructing a highly integrated, functionally synergistic composite material system.

The XRD diffraction patterns of aerogel (GA) and GA/Ni-CN matrix materials are shown in Figure **3**(**a**). GA/Ni-CN exhibits diffraction peaks of varying intensities near 26°, 44°, and 52°, corresponding to the characteristic (002) plane of the carbon material and the characteristic (111) and (200) planes of Ni, respectively [1, 5]. This indicates the successful incorporation of the nickel metal catalyst into the support material. Thermal gravimetric analysis (TGA) was conducted on the S@GA/Ni-CN composite material obtained after adsorption of sulfur onto GA/Ni-CN (see Figure **3b**). The sulfur content within the S@GA/Ni-CN composite was determined through TGA experiments (Figure **3b**). shows that significant weight loss begins when the test temperature rises from room temperature to 150 °C. At 350 °C, the mass no longer decreases. Within the aforementioned temperature range, the weight loss rate of the sulfur-containing composite material is approximately 71%, indicating that the mass fraction of sulfur in the material is about 71%. This value aligns well with the 7:3 sulfur-to–GA/Ni-CN mass ratio introduced during the experiment.

The adsorption/desorption test curve of the GA/Ni-CN composite material is shown in Figure **3c**. The curve exhibits a Type I isotherm, indicating that this carbon-based composite material possesses a microporous structure, which corresponds to the pore size distribution curve of the material in Figure **3d**. The BET method theoretical calculation from surface adsorption experiments yielded a specific surface area of 2135.017 m^2/g and a pore volume of 1.244 cm^3/g for GA/Ni-CN. As shown in Figure **3d**, the pore sizes of this composite material are predominantly concentrated between 1.0 nm and 3 nm, with an average pore size of approximately 1.68 nm. The abundant pore structure and high specific surface area enhance the contact area between the host material

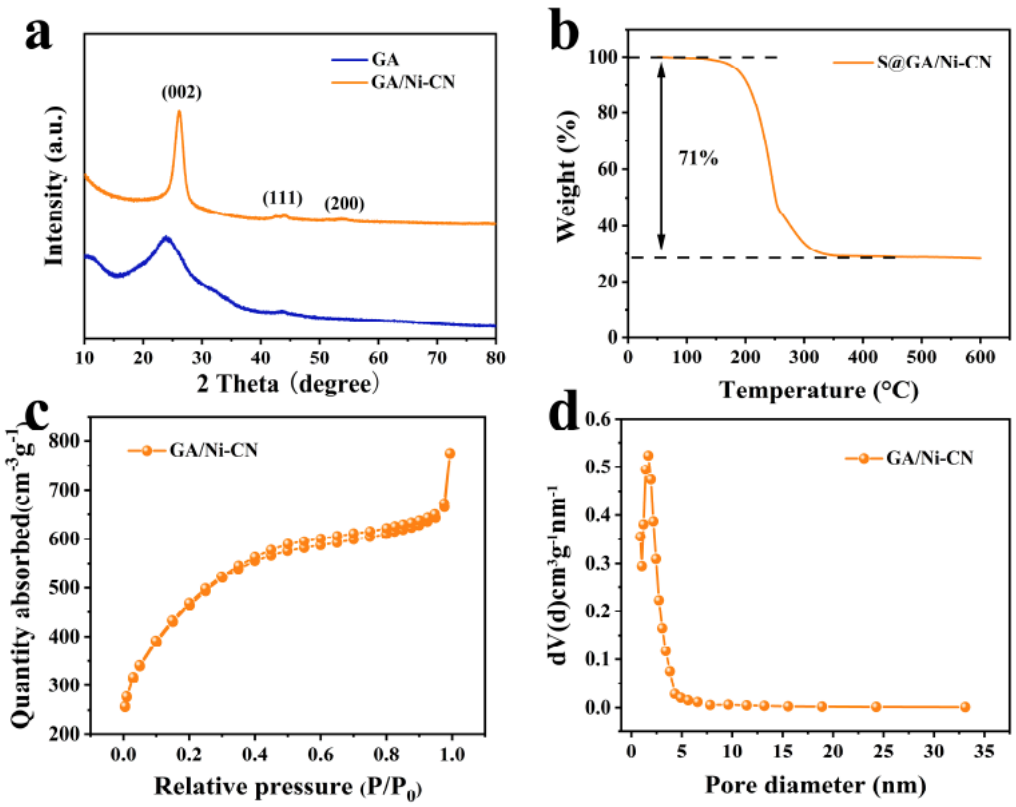

Figure 3: (**a**) XRD patterns of GA and GA/Ni-CN. (**b**) TGA curve of S@GA/Ni-CN. (**c**) Nitrogen adsorption and desorption curves of GA/Ni-CN. (**d**) Pore size distribution of GA/Ni-CN.

and the active substance, thereby improving its reactivity and accelerating the conversion process of polysulfides [41].

2.2. Electrochemical Performance

A 2023-type button cell was assembled in a glove box filled with high-purity argon gas, utilizing S@GA/Ni-CN composite material as the cathode active material and metallic lithium foil as the anode. The cyclic voltammetry (CV) results are shown in Figure **4a**. A distinct oxidation peak appears at 2.38 V, corresponding to the conversion of Li_2S to S[1]. Two reduction peaks are observed at 2.31 V and 2.02 V, corresponding to the conversion of S to Li_2S_x and LiSx to Li_2S, respectively [5]. In contrast, the CV curve of the S@GA material—obtained by adsorbing sulfur onto bare GA—exhibited weaker peak intensities and varying degrees of peak shift. This indicates lower polarization and faster redox kinetic response for S@GA/Ni-CN. The lithium ions diffusion coefficient provides an intuitive measure of the conversion rate of active species; a higher value signifies greater conversion efficiency of lithium polysulfides. To determine the influence of the Ni catalyst on electrode redox reaction kinetics, CV tests were conducted on both S@GA and S@GA/Ni-CN electrodes at different scan rates (as shown in Figure **4b-c**). In the CV curves, the peak current of the oxidation peak is labeled I_A, while the peak currents of the reduction peaks are labeled I_{C1} and I_{C2}. It is evident that the peak currents of both electrodes increase with rising scan rates. Compared to the S@GA electrode material, the S@GA/Ni-CN electrode material exhibits higher peak currents. According to the Randles-Sevcik equation [1, 5, 42, 43]:

$$I_P=(2.69\times10^5)n^{1.5}SD_{Li+}{}^{0.5}\Delta C_{Li+}v^{0.5} \quad (1)$$

In the equation, IP and v represent the peak current and scan rate, respectively, in the CV curve. Since the number of electron transfers (n), the geometric area of the sulfur electrode (S), and the lithium ions concentration (C Li^+) are all constant values, the peak current (I_A) of the oxidation peak and the peak currents (I_{C1}, I_{C2}) of the reduction peaks (C1, C2) exhibit a linear relationship with the square root of the scan rate [1]. Therefore, the lithium ions diffusion rate (D Li^+) for S@GA and S@GA/Ni-CN is determined by the slope of the fitted line ($I/v^{0.5}$) [44] (as shown in Figure **4d-f**).

Based on the slopes of the fitted lines in Figure **4d-f**, the lithium ions diffusion rates for all peaks in the S@GA/Ni-CN electrode material are significantly higher than those in the S@GA electrode material. This indicates that the introduction of the Ni catalyst accelerates the lithium ions transport rate, enabling the battery to achieve a higher lithium ions transport flux. Consequently, this promotes electron migration and the

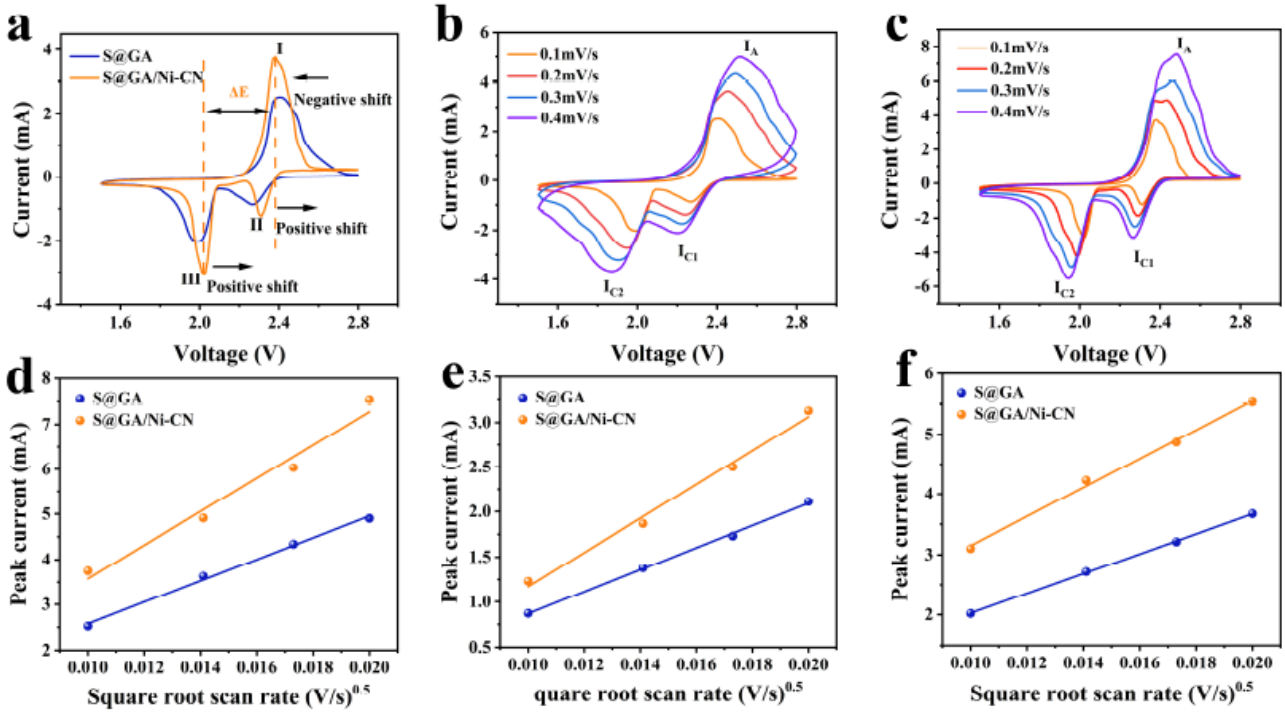

Figure 4: (**a**) CV curves of S@GA and S@GA/Ni-CN electrodes at 0.1 mV/s. (**b**) The CV curves of S@GA electrode and (**c**) S@GA/Ni-CN electrode at scanning rates of 0.1-0.4 mV/s. (**d**) oxidation peak and reduction peak corresponding fit plots of the peak currents of (**e**) C1 and (**f**) C2 versus the square root of the scan rate.

conversion of polysulfides, resulting in more stable long-term cycling performance for the Li-S battery.

Figure **5a** shows the electrochemical impedance spectroscopy (EIS) curves and corresponding circuit impedance simulations for the S@GA and S@GA/Ni-CN electrodes. The EIS curves exhibit semicircular arcs at high frequencies and straight lines at low frequencies, corresponding to the charge transfer resistance (R_{ct}) and ionic diffusion resistance (R_0) of the electrode materials, respectively [1, 44] As shown in Figure **5a**, the S@GA electrode exhibits R_{ct} and R_0 values of 51 Ω and 16 Ω, respectively. In contrast, the S@GA/Ni-CN electrode exhibits a smaller semicircular diameter, with R_{ct} and R_0 values of 35 Ω and 8.27 Ω, respectively. This indicates that the introduction of the nickel catalyst reduces the impedance of the composite electrode material, enhances ion migration rates, and accelerates the redox reaction process [1, 45]. Additionally, to evaluate the specific capacity of the different electrodes, we performed galvanostatic charge-discharge (GCD) tests at a 0.2 C (as shown in Figure **5b**). Both electrodes exhibited GCD curves with two discharge plateaus and one charge plateau, corresponding to two reduction peaks and one oxidation peak in the cyclic voltammetry curves. The S@GA/Ni-CN electrode displayed longer charge and discharge plateaus, indicating higher specific capacity.

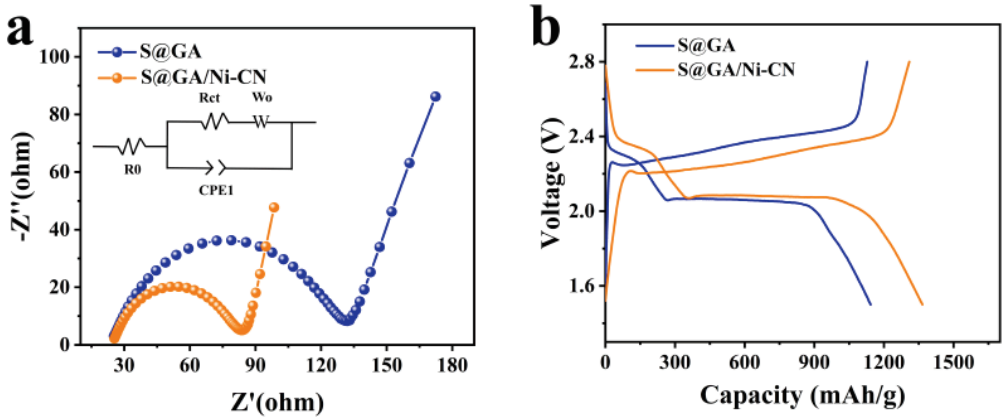

Figure 5: (**a**) EIS curves of S@GA and S@GA/Ni-CN electrodes. (**b**) Charge/discharge curves of S@GA and S@GA/Ni-CN electrodes at the rate of 0.2 C.

The performance tests of two electrode materials (S@GA and S@GA/Ni-CN) at different rates of 0.2, 0.3, 0.5, 1, and 2 C are shown in Figure **6a**. It can be seen that the initial discharge specific capacity of S@GA/Ni-CN at 0.2 C reaches 1365.3 mAh/g. As the current density further increases, the battery capacity also continuously decreases. When the current density was 2 C, the discharge specific capacity of S@GA/Ni-CN is 536.7 mAh/g. Subsequently, when the current density further decreased to 0.2 C, the discharge specific capacity of the S@GA/Ni-CN electrode material recovered to 1190 mAh/g. In contrast, the discharge specific capacity of S@GA electrode material at 0.2 C is only 1143.1 mAh/g. As the current density further increases, the degradation of battery capacity also increases significantly. When the current density further increases to 2 C, the discharge specific capacity of S@GA battery drops to 288.4 mAh/g; It can be seen that there is a significant difference in capacity between the two electrode materials when discharged at high or low rates.

Figures **6b-c** show the charge-discharge curves of S@GA and S@GA/Ni-CN batteries at different rates. It is evident that the discharge capacity gradually decreases with increasing charge-discharge current, attributed to the corresponding increase in electrode polarization. At lower charge/discharge current densities, both S@GA and S@GA/Ni-CN electrodes exhibit more pronounced charge/discharge plateaus. When the applied current density reaches 2 C, the charge/discharge performance of S@GA degrades more rapidly. This is because lithium polysulfides cannot be rapidly converted at higher currents, leading to a reduction in the battery's specific capacity. In contrast, S@GA/Ni-CN maintains a higher discharge specific capacity than S@GA even at elevated current densities, indicating that the incorporation of Ni nanoparticles enhances electrochemical reactivity. Figure **6d** compares the overpotentials of both electrodes at different current densities. As current density increases, the overpotential of the S@GA electrode is significantly higher than that of the S@GA/Ni-CN electrode. This indicates greater polarization within the battery assembled with S@GA, indicating more severe polarization. Collectively, these results confirm that the introduction of the nickel catalyst effectively accelerates polysulfide conversion, thereby improving the electrochemical kinetics of the electrode.

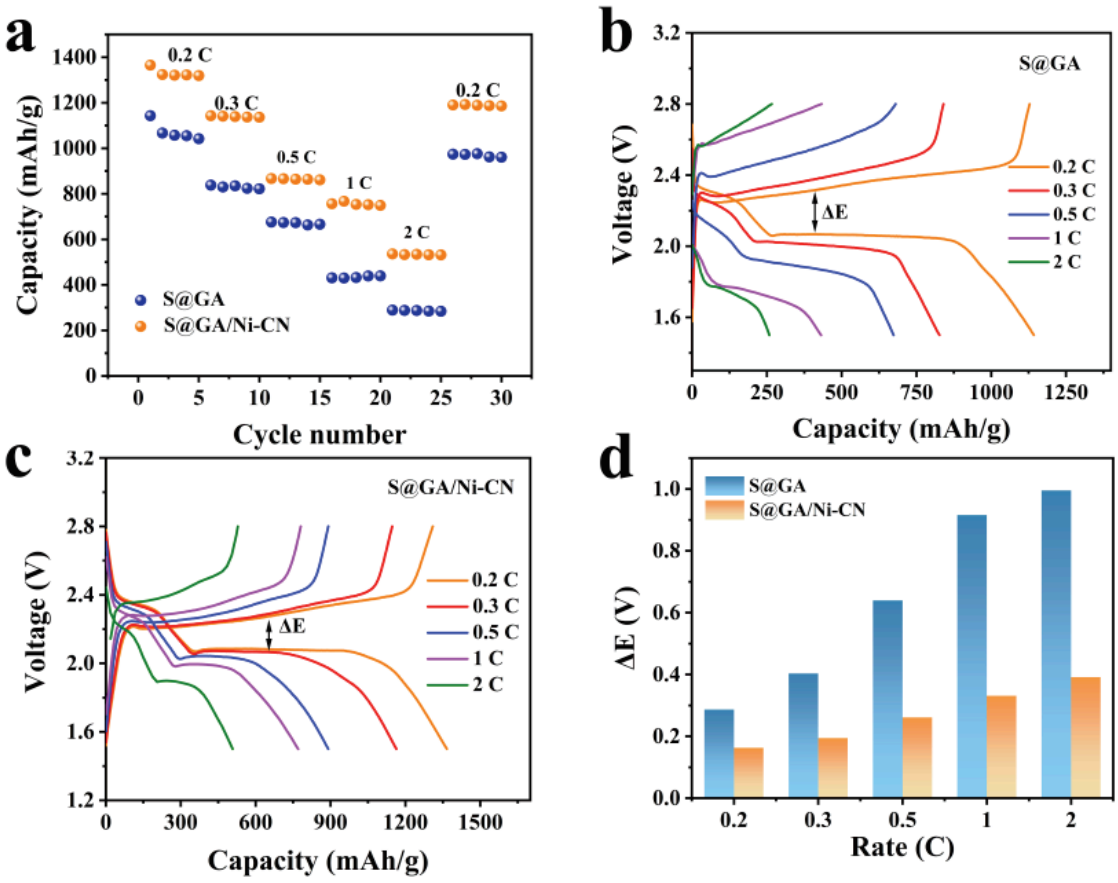

Figure 6: (a) The rates performance of S@GA and S@GA/Ni-CN electrodes. (b) Charge/discharge curves of S@GA electrode at different rates. (c) Charge/discharge curves of S@GA/Ni-CN electrode at different rates. (d) The overpotential of S@GA and S@GA/Ni-CN electrodes at different rates.

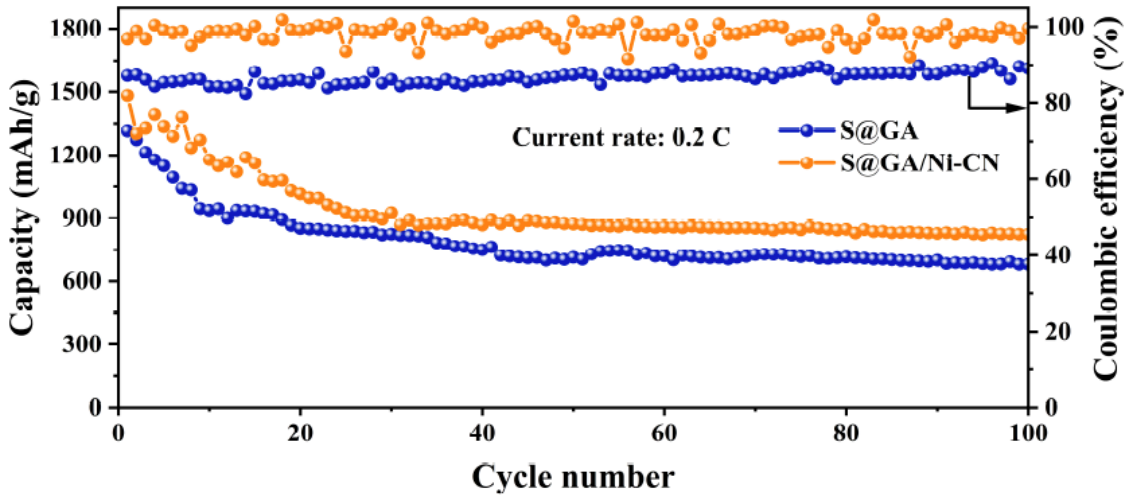

Figure 7: Cycling performance of S@GA and S@GA/Ni-CN electrodes at 0.2 C rate.

To further characterize the cycling stability of S@GA and S@GA/Ni-CN electrodes at 0.2 C rate, we conducted 100 long-cycle tests on both electrodes (as shown in Figure **7**). The S@GA and S@GA/Ni-CN electrode exhibited an initial discharge specific capacity of 1482 mAh/g. After 25 cycles, its decay rate gradually leveled off, with a reversible capacity of 824.6 mAh/g after 100 cycles. S@GA exhibited an initial discharge specific capacity of 1316 mAh/g at 0.2 C. After 100 cycles, its reversible capacity decreased to 679.2 mAh/g. These results clearly demonstrate that S@GA/Ni-CN provides a substantially higher specific capacity, both initially and after extended cycling, along with improved coulombic efficiency relative to S@GA. From the perspective of sustainability and environmental impact, the GA/Ni-CN composite exhibits certain advantages in green composite research. This system, primarily composed of carbon materials, possesses potential for recycling or reuse after the depletion of sulfur active material. Additionally, the low nickel loading contributes to reducing the environmental burden associated with critical metals. Furthermore, this synthesis strategy demonstrates good compatibility with existing electrode recycling processes and can be extended to renewable or biomass-derived carbon precursors, providing a viable pathway for designing environmentally friendly composite materials.

Biodegradable polymers and bio-based matrices offer distinct advantages in terms of renewability and environmental friendliness. However, under the demanding electrochemical operating conditions of lithium-sulfur batteries, they often suffer from limited electrical conductivity, insufficient chemical stability, and inadequate structural strength. In contrast, the carbon-based GA/Ni-CN composite forms a framework structure that combines high conductivity with excellent mechanical toughness, making it more suitable for long-term electrochemical operation. Crucially, the composite design approach in this work does not exclude sustainability considerations. This structure is compatible with future hybrid systems combining biomass-derived carbon sources or conductive carbon frameworks with degradable components, thereby establishing its relevance in the field of green and sustainable composite materials research. More importantly, as a continuous framework structure with excellent mechanical toughness, the nitrogen-doped carbon derived from MOFs further enhances the strength of the three-dimensional graphene aerogel and improves interfacial bonding stability. The tight integration among all components helps maintain the overall structural integrity during electrode fabrication and repeated electrochemical cycling. This supplementary discussion strengthens the paper's contribution in the field of composite materials.

3. CONCLUSION

Through freeze-drying and sol-gel methods, metallic nickel was successfully loaded onto porous carbon materials. The resulting GA/Ni-CN matrix exhibits excellent conductivity, facilitating rapid electron migration. Its high surface area and abundant pore structure provide additional adsorption sites, accelerating the conversion of lithium polysulfides and thereby suppressing the shuttle effect in Li-S batteries. This system, primarily composed of carbon materials, possesses potential for recycling or reuse after depletion of sulfur-based active materials. Furthermore, the low nickel loading contributes to reducing the environmental burden associated with critical metals. Furthermore, this synthesis strategy demonstrates good compatibility with existing electrode recycling

processes and can be extended to renewable or biomass-derived carbon precursors, providing a viable pathway for designing environmentally friendly composite materials. As a consequence, the S@GA/Ni-CN composite cathode demonstrates superior electrochemical performance, delivering an initial discharge capacity of 1482 mAh/g at 0.2 C and retaining 824.6 mAh/g after 100 cycles, demonstrating excellent capacity retention and cycling stability.

4. EXPERIMENTAL

4.1. Materials and Testing Instruments

Zinc nitrate hexahydrate ($Zn(NO_3)_2·6H_2O$), 2-methylimidazole, sulfur powder, nickel acetate ($Ni(CH_3COO)_2$), and N-methyl-2-pyrrolidone were purchased from Aladdin Company (analytical grade); methanol solution was purchased from Sinopharm Group (analytical grade); SuperP was purchased from LION Corporation, Japan (battery grade); PVDF was purchased from Arkema, France (battery grade). Lithium/sulfur battery electrolyte was purchased from Duoduo Reagent (battery grade); polypropylene membrane (Celgard 2400) was purchased from Celgard, USA (battery grade).

Ultima IV X-ray Diffractometer (XRD), Rigaku Corporation, Japan; Regulus 8100 Scanning Electron Microscope (SEM), Hitachi, Ltd., Japan; ASIQ A3501-5 Fully Automated Gas Adsorption Analyzer, Kanta Instruments, Inc., USA; Chi 760 Electrochemical Workstation, Shanghai Chenhua; Charge-Discharge Tester, Wuhan Lande Electronics Co., Ltd.

4.2. Sample Preparation

4.2.1. Preparation of GA Material

Transfer 5 mL of a 10 mg/mL graphene oxide solution into a beaker. Add ascorbic acid in a 1:1 mass ratio, followed by a slow addition of a 50 mg/mL sodium dodecyl sulfate (SDS) solution. Stir thoroughly, then immediately place the beaker in an oven. React at 80 °C for 2 hours. Subsequently, transfer the mixture to a -20 °C freezer for 8 hours of cooling. Then, place the material in a 95 °C oven for a further 6 hours of reaction. After removal, wash the material at least three times with anhydrous ethanol and deionized water. Dry thoroughly, then transfer to a tube furnace. Under a protective N_2 atmosphere, heat at a rate of 5 °C/min to 930 °C. Maintain this temperature for 3 hours of carbonization treatment. Allow the material to cool naturally to room temperature to obtain a three-dimensional black gas-sintered (GA) ultralight porous material.

4.2.2. Preparation of GA/Ni-ZIF-8 Materials

Separately take 6.568 g of 2-methylimidazole, 4.8 g of $Zn(NO_3)_2·6H_2O$, 0.35 g of nickel acetate, and 1.6 g of pre-carbonized GA material were dissolved in 120 mL of methanol solution. A 1 mL aliquot of 50 mg/mL SDS solution was added dropwise, and the mixture was stirred thoroughly before transfer to a high-pressure reactor lined with polytetrafluoroethylene. The mixture reacted at 120 °C for 4 hours. After centrifugation, washing, and vacuum drying, the GA/Ni-ZIF-8 composite material was obtained.

4.2.3. Preparation of GA/Ni-CN Material

The dried GA/Ni-ZIF-8 material was transferred to a tube furnace. Under N_2 atmosphere protection, it was heated at a rate of 5 °C/min to 930 °C and subjected to high-temperature carbonization for 3 h. After natural cooling to room temperature, the black solid product GA/Ni-CN was obtained. It is worth noting that the precursor material for synthesizing GA is graphite, which is relatively inexpensive and abundant in reserves. And the synthesis process of composite materials is relatively simple, with only a small amount of SDS added as a surfactant, which has little impact on the environment.

4.2.4. Preparation of S@GA/Ni-CN and S@GA Materials

GA/Ni-CN was mixed with sulfur powder at a 3:7 mass ratio, then transferred to a reactor and heated at 155 °C for 12 h. After natural cooling, the S@GA/Ni-CN black solid material was obtained. The synthesis of S@GA material followed the same procedure as above, except GA/Ni-CN was replaced with GA.

4.3. Preparation of Electrode Materials

The electrode active material (S@GA/Ni-CN), conductive agent (Super P), and binder (PVDF) were mixed and ground at a mass ratio of 7:2:1. An appropriate amount of N-methyl-2-pyrrolidone (NMP) was then added, and the mixture was stirred for 12 h. Using a coating squeegee, uniformly coat the S@GA/Ni-CN electrode paste onto clean aluminum foil and dry in a vacuum oven at 60 °C for over 12 hours. Finally, cut into circular electrode discs with a diameter of 13 mm using a slicer. The sulfur loading per electrode disc is approximately 1.5 mg/cm².

4.4. Battery Assembly

Assemble into CR2032 button cells within a glove box filled with high-purity argon, where oxygen and moisture levels are both below 0.1 ppm. The prepared electrode discs served as the cathode, with metallic

lithium foil as the anode. Celgard 2400 polypropylene membrane was used as the separator, and the electrolyte consisted of 1.0 M LiTFSI dissolved in DOL/DME (V/V=1:1 + 2.0 wt% $LiNO_3$).

4.5. Electrochemical Performance Testing

Cyclic voltammetry (CV, 1.5–2.8 V) and electrochemical impedance spectroscopy (EIS, 0.1 Hz–100 kHz) were performed using a Chi760 electrochemical workstation. Charge-discharge performance testing was conducted within the 1.5–2.8 V voltage range using a BlueCharge battery tester.

CONFLICT OF INTEREST STATEMENT

The authors declare that they have no known competing financial interests or personal relationships that could have appeared to influence the work reported in this paper.

DATA AVAILABILITY

The data that has been used is confidential.

ACKNOWLEDGMENTS

The work described in this paper was supported by the National Key Research and Development Program of China (2022YFB3704700, 2022YFB3704702), the Major Scientific and Technological Innovation Project of Shandong Province (2021CXGC010901) and the Taishan Scholar Program of Shandong Province (TS201511031) and the Taishan Industrial Experts Program of Shandong Province (tsls20241105).

REFERENCES

[1] Lu, J.; Zhu, M.; Kim, M.; He, A.; Wang, C.; Kim, T. H.; Lee, S. H. Catalytic nickel nanoparticles embedded on ZIF-8 backbone for accelerating polysulfide conversion in lithium-sulfur batteries. J. Power Sources 2025, 647, 237269. https://doi.org/10.1016/j.jpowsour.2025.237269

[2] Li, H.; Li, L.; Li, X.; Ou, Y.; Yuan, W. Stepwise regulation of polysulfide conversion by in situ constructed ZnSe-$MoSe_2$ heterojunctions in N-doped hollow carbon nanocages for lithium-sulfur batteries. Applied Catalysis B: Environment and Energy 2025, 125631. https://doi.org/10.1016/j.apcatb.2025.125631

[3] Chen, Y.; Wang, T.; Tian, H.; Su, D.; Zhang, Q.; Wang, G. Advances in lithium–sulfur batteries: from academic research to commercial viability. Adv. Mater. 2021, 33 (29), 2003666. https://doi.org/10.1002/adma.202003666

[4] Zuo, Y. Z.; Ren, P. J.; Zhao, M.; Su, W. M.; Chen, Y. B.; Tang, Y. F.; Chen, Y. F. Stable lithium-sulfur batteries with high sulfur content fabricated by ultralight ochroma lagopus-derived carbon with dopamine shell as sulfur host. J. Alloy. Compd. 2020, 819, 10. https://doi.org/10.1016/j.jallcom.2019.152995

[5] Lu, J.; Zhu, M.; Wang, C.; Wang, L.; Wu, C.; Cui, Y.; Bi, Q.; Jiang, S.; Zhao, Q.; Li, X. Nitrogen-doped 3D porous composite GA/HNBRL used as a self-supporting electrode to enhance the adsorption and conversion of polysulfide in high-capacity Li–S batteries. ACS Sustainable Chemistry & Engineering 2025, 13, 5c06841. https://doi.org/10.2139/ssrn.5225891

[6] Wang, C.; Song, H.; Yu, C.; Ullah, Z.; Guan, Z.; Chu, R.; Zhang, Y.; Zhao, L.; Li, Q.; Liu, L. Iron single-atom catalyst anchored on nitrogen-rich MOF-derived carbon nanocage to accelerate polysulfide redox conversion for lithium sulfur batteries. J. Mater. Chem. A 2020, 8 (6), 3421-3430. https://doi.org/10.1039/C9TA11680J

[7] Chu, R.; Nguyen, T. T.; Bai, Y.; Kim, N. H.; Lee, J. H. Uniformly controlled treble boundary using enriched adsorption sites and accelerated catalyst cathode for robust lithium–sulfur batteries. Adv. Energy Mater. 2022, 12 (9), 2102805. https://doi.org/10.1002/aenm.202102805

[8] Luo, X; Pu, Z; Li, H; Li, Z; Yang, X; Fu, A; Li, H. Co_2P nanoparticles decorated porous carbon nanofibers as self-standing cathode for high-performance Li–S batteries. ACS Appl. Mater. Interfaces 2025, 17, 26, 38019–38030. https://doi.org/10.1021/acsami.5c06263

[9] Yu, B.; Chen, D.; Wang, Z.; Qi, F.; Zhang, X.; Wang, X.; Hu, Y.; Wang, B.; Zhang, W.; Chen, Y. Mo_2C quantum dots@ graphene functionalized separator toward high-current-density lithium metal anodes for ultrastable Li-S batteries. Chem. Eng. J. 2020, 399, 125837. https://doi.org/10.1016/j.cej.2020.125837

[10] Ye, Z.; Jiang, Y.; Li, L.; Wu, F.; Chen, R. A high-efficiency CoSe electrocatalyst with hierarchical porous polyhedron nanoarchitecture for accelerating polysulfides conversion in Li–S batteries. Adv. Mater. 2020, 32 (32), 2002168. https://doi.org/10.1002/adma.202002168

[11] Wang, J. N.; Yi, S. S.; Liu, J. W.; Sun, S. Y.; Liu, Y. P.; Yang, D. W.; Xi, K.; Gao, G. X.; Abdelkader, A.; Yan, W.; et al. Suppressing the shuttle effect and dendrite growth in lithium-sulfur batteries. ACS Nano, 2020, 14 (8), 9819-9831. https://doi.org/10.1021/acsnano.0c02241

[12] Luo, X; Pu, Z; Li, H; Zhao, E; Yang, X; Fu, A; Li, H. Preparation of TiO_2 nanoparticles decorated porous carbon via a pseudo co-templating strategy and their application as substrates for high performance cathode of Li-S batteries. J. Energy Storage 2024, 102, 114219. https://doi.org/10.1016/j.est.2024.114219

[13] Liang, Z.; Shen, J.; Xu, X.; Li, F.; Liu, J.; Yuan, B.; Yu, Y.; Zhu, M. Advances in the development of single-atom catalysts for high-energy-density lithium–sulfur batteries. Adv. Mater. 2022, 34 (30), 2200102. https://doi.org/10.1002/adma.202200102

[14] Liu, J.; Lin, C.; Xie, Q.; Peng, D. L.; Xie, R. J. Core–shell zeolite imidazole framework-derived ZnSe@ $CoSe_2$/C heterostructure enabling robust polysulfide adsorption and rapid Li^+ diffusion in high-rate and high-loading lithium–sulfur batteries. Chem. Eng. J. 2022, 430, 133099. https://doi.org/10.1016/j.cej.2021.133099

[15] Fan, W.; Chu, R.; Wang, C.; Song, H.; Ding, Y.; Li, X.; Jiang, M.; Li, Q.; Liu, L.; He, A. Synthesis and characteristic of the ternary composite electrode material PTCDA/CNT@ MPC and its electrochemical performance in sodium ion battery. Composites Part B: Engineering 2021, 226, 109329. https://doi.org/10.1016/j.compositesb.2021.109329

[16] Li, H.; Wang, Z.; Dang, L.; Yu, K.; Yang, R.; Fu, A.; Liu, X.; Guo, Y.-G.; Li, H.; Zhao, X. S. Si nanoparticles enclosed in hierarchically structured dual-component porous carbon as superior anode for lithium-ion batteries: structure formation and properties investigation. Energy Storage Mater. 2024, 70, 103547. https://doi.org/10.1016/j.ensm.2024.103547

[17] Bai, Y. Q.; Wang, C. G.; Li, X.; Fan, W. Q.; Song, P. H.; Gu, Y. C.; Liu, F. Q.; Liu, G. Y. Preparation and electrochemical properties of S@C composite material with high capacity and ordered alignment of channels. Chemical J ournal of Chinese Universities 2020, 41, 1306-1312.

[18] Ren, Z.; Li, J.; Gong, Y.; Li, X.; Liang, J.; Li, Y.; He, C.; Zhang, Q.; Ren, X. Efficient capture and conversion of polysulfides by zinc protoporphyrin framework-embedded triple-layer nanofiber separator for advanced Li-S batteries. Journal of

Colloid and Interface Science 2022, 609, 43-53. https://doi.org/10.1016/j.jcis.2021.12.003

[19] Shi, M.; Liu, Z.; Zhang, S.; Liang, S.; Jiang, Y.; Bai, H.; Jiang, Z.; Chang, J.; Feng, J.; Chen, W. A Mott–Schottky heterogeneous layer for Li–S batteries: enabling both high stability and commercial-sulfur utilization. Adv. Energy Mater. 2022, 12 (14), 2103657. https://doi.org/10.1002/aenm.202103657

[20] Wang, M. Y.; Bai, Z. C.; Yang, T.; Nie, C. H.; Xu, X.; Wang, Y. X.; Yang, J.; Dou, S. X.; Wang, N. N. Advances in high sulfur loading cathodes for practical lithium-sulfur batteries. Adv. Energy Mater. 2022, 12 (39), 25. https://doi.org/10.1002/aenm.202201585

[21] Wang, Z. K.; Li, Y.; Ji, H. Q.; Zhou, J. Q.; Qian, T.; Yan, C. L. Unity of opposites between soluble and insoluble lithium polysulfides in lithium-sulfur batteries. Adv. Mater. 2022, 34 (47), 17. https://doi.org/10.1002/adma.202203699

[22] Wu, Y.; Li, D.; Pan, J.; Sun, Y.; Huang, W.; Wu, M.; Zhang, B.; Pan, F.; Shi, K.; Liu, Q. Realizing fast polysulfides conversion within yolk-shelled NiO@HCSs nanoreactor as cathode host for high-performance lithium-sulfur batteries. J. Mater. Chem. A 2022, 10 (30), 16309-16318. https://doi.org/10.1039/D2TA03421B

[23] Xiang, M.; Li, J.; Feng, S.; Zhang, H.; Cao, X.; Zeng, Y.; Li, X.; Xiao, J. Synergistic capture and conversion of polysulfides in cathode composites with multidimensional framework structures. Journal of Colloid and Interface Science 2022, 624, 471-481. https://doi.org/10.1016/j.jcis.2022.05.118

[24] Yang, X. Y.; Li, R.; Yang, J. X.; Liu, H. Z.; Luo, T.; Wang, X. L.; Yang, L. A novel route to constructing high-efficiency lithium sulfur batteries with spent graphite as the sulfur host. Carbon 2022, 199, 215-223. https://doi.org/10.1016/j.carbon.2022.06.067

[25] Zhang, W.; Hong, D.; Su, Z.; Yi, S.; Tian, L.; Niu, B.; Zhang, Y.; Long, D. Tailored ZnO-ZnS heterostructure enables a rational balancing of strong adsorption and high catalytic activity of polysulfides for Li-S batteries. Energy Storage Mater. 2022, 53, 404-414. https://doi.org/10.1016/j.ensm.2022.09.018

[26] Bai, Y.; Nguyen, T. T.; Chu, R.; Song, H.; Kim, N. H.; Lee, J. H. Heterostructured TiN/TiO_2 on the hierarchical N-doped carbon for enhancing the polysulfide immobilization and sulfur reduction in lithium-sulfur battery. Chem. Eng. J. 2023, 476, 146581. https://doi.org/10.1016/j.cej.2023.146581

[27] Chu, R.; Nguyen, T. T.; Song, H.; Austeria, M.; Bai, Y.; Kim, D. H.; Lee, J. H.; Kim, N. H. Crystal transformation engineering for effective polysulfides blocking layer for excellent energy density lithium–sulfur batteries. Energy Storage Mater. 2023, 61, 102877. https://doi.org/10.1016/j.ensm.2023.102877

[28] Deng, R.; Yu, H.; Liu, J.; Chu, F.; Lei, J.; Yang, L.; Wu, F. Adsorption-catalytic effects of metallurgical ferrous slag on polysulfides in Li–S batteries. J. Mater. Chem. A 2023, 11 (29), 15769-15777. https://doi.org/10.1039/D3TA02327C

[29] Feng, P.; Hou, W.; Bai, Z.; Bai, Y.; Sun, K.; Wang, Z. Ultrathin two-dimensional bimetal NiCo-based MOF nanosheets as ultralight interlayer in lithium-sulfur batteries. Chinese Chemical Letters 2023, 34 (4), 107427. https://doi.org/10.1016/j.cclet.2022.04.025

[30] Feng, S.; Wang, J.; Wen, J.; Li, X.; Wang, Z.; Zeng, Y.; Xiao, J. Improvement of redox kinetics of dendrite-free lithium–sulfur battery by bidirectional catalysis of cationic dual-active sites. ACS Sustainable Chemistry & Engineering 2023, 11 (23), 8544-8555. https://doi.org/10.1021/acssuschemeng.3c01158

[31] Hao, Q.; Qian, X.; Jin, L.; Cheng, J.; Zhao, S.; Chen, J.; Zhang, K.; Li, B.; Pang, S.; Shen, X. Application of ZIF-67/ZIF-8 derived Co_3O_4/ZnO heterojunction in lithium-sulfur battery separators. J. Alloy. Compd. 2023, 967, 171605. https://doi.org/10.1016/j.jallcom.2023.171605

[32] Li, T.; Liang, L.; Chen, Z.; Zhu, J.; Shen, P. Hollow $Ti_3C_2T_x$ MXene@ $CoSe_2$/N-doped carbon heterostructured composites for multiphase electrocatalysis process in lithium-sulfur batteries. Chem. Eng. J. 2023, 474, 145970. https://doi.org/10.1016/j.cej.2023.145970

[33] Qin, B.; Zhao, X.; Wang, Q.; Yao, W.; Cai, Y.; Chen, Y.; Wang, P.; Zou, Y.; Cao, J.; Zheng, X. A tandem electrocatalyst with dense heterointerfaces enabling the stepwise conversion of polysulfide in lithium-sulfur batteries. Energy Storage Mater. 2023, 55, 445-454. https://doi.org/10.1016/j.ensm.2022.12.014

[34] Song, P.; Zheng, S.; Ullah, Z.; Yang, Z.; Zhu, P.; He, A.; Wang, C.; Li, Q. Synergistic effects of FeCo bimetallic single-atom catalysts: accelerating the redox conversion of polysulfides and inhibiting the growth of lithium dendrites in lithium–sulfur batteries. ACS Applied Energy Materials 2023, 6 (9), 4671-4682. https://doi.org/10.1021/acsaem.2c04118

[35] Xiao, W.; Kiran, G. K.; Yoo, K.; Kim, J. H.; Xu, H. The dual-site adsorption and high redox activity enabled by hybrid organic-inorganic vanadyl ethylene glycolate for high-rate and long-durability lithium–sulfur batteries. Small 2023, 19 (20), 2206750. https://doi.org/10.1002/smll.202206750

[36] Zhou, Q. Y.; Tan, L.; Lv, T. B.; Li, M. C.; Zhang, J. J.; Zhao, Z. Q.; Jin, X. J.; Liu, Z.; Hou, P. P.; Zeng, Z. Nickel foam coated by Ni nanoparticle-decorated 3D nanocarbons as a freestanding host for high-performance lithium–sulfur batteries. ACS Appl. Mater. Interfaces 2023, 15 (2), 3037-3046. https://doi.org/10.1021/acsami.2c19987

[37] Das, S.; Bhuyan, M.; Gupta, K. N.; Okpowe, O.; Choi, A.; Sweeny, J.; Olawale, D.; Pol, V. G. Optimization of the form factors of advanced Li-S pouch cells. Small 2024, 20 (31), 2311850. https://doi.org/10.1002/smll.202311850

[38] Zhang, W.; He, X.; He, C. The “dp orbital hybridization”-guided design of novel two-dimensional MOFs with high anchoring and catalytic capacities in Lithium−Sulfur batteries. Journal of Colloid and Interface Science 2025, 678, 540-548. https://doi.org/10.1016/j.jcis.2024.08.184

[39] Wang, S. Y.; Wang, Z. W.; Chen, F. Z.; Peng, B.; Xu, J.; Li, J. Z.; Lv, Y. H.; Kang, Q.; Xia, A. L.; Ma, L. B. Electrocatalysts in lithium-sulfur batteries. Nano Res. 2023, 16 (4), 4438-4467. https://doi.org/10.1007/s12274-022-5215-4

[40] Wang, T.; He, J.; Zhu, Z.; Cheng, X. B.; Zhu, J.; Lu, B.; Wu, Y. Heterostructures regulating lithium polysulfides for advanced lithium-sulfur batteries. Adv. Mater. 2023, 35 (47), 2303520. https://doi.org/10.1002/adma.202303520

[41] Zhang, Y.; Wang, M.; Chen, B.; Zeng, W.; Liu, Y.; Yang, H.; Huang, J.; Zhou, M. Win-win cooperation of boron-doped C_3N_5 porous nanosheets and $CoSe_2$ nanorods for promoting cathodic sulfur conversion in lithium–sulfur batteries. Chem. Eng. J. 2025, 510, 161776. https://doi.org/10.1016/j.cej.2025.161776

[42] Han, F.; Yan, D.; Guan, X.; Lu, Q.; Yin, S.; Yan, Y.; Zhou, H.; Yang, P.; Zhang, Q.; Zhang, S. Self-assembled 3D CoSe-based sulfur host enables high-efficient and durable electrocatalytic conversion of polysulfides for flexible lithium-sulfur batteries. Energy Storage Mater. 2024, 71, 103652. https://doi.org/10.1016/j.ensm.2024.103652

[43] Chu, R.; Nguyen, T. T.; Song, H.; Bai, Y.; Tran, D. T.; Kim, N. H.; Lee, J. H. Enriched vacancies of ruthenium doped niobium oxide on hollow graphene sphere as sulfur reduction reaction promoter in lithium sulfur batteries. Applied Catalysis B: Environment and Energy 2024, 352, 124030. https://doi.org/10.1016/j.apcatb.2024.124030

[44] Song, H.; Nguyen, T. T.; Chu, R.; Bai, Y.; Kim, N. H.; Lee, J. H. Coupling interfacial effect in heterogeneous RuP_2-RuP for accelerating sulfur reduction reaction of lithium sulfur batteries. Nano Energy 2024, 109859. https://doi.org/10.1016/j.nanoen.2024.109859

[45] Wang, H. Y.; Dai, Y. K.; Liao, K. M.; Deng, S.; Dai, G. P. Vertical graphene growth on LDH nanosheets and carbon cloth nanofibers with NiCo nanoparticles as a freestanding host for high-performance lithium–sulfur batteries. The Journal of Physical Chemistry Letters 2025, 16 (4), 1103-1113. https://doi.org/10.1021/acs.jpclett.4c03506

https://doi.org/10.12974/2311-8717.2025.13.13